Fracture Quality from Integrating Time-Lapse VSP and Microseismic Data

Mark E. Willis, Daniel R. Burns, Rongrong Lu, M. Nafi Toksöz,
Earth Resources Laboratory
Dept. of Earth, Atmospheric, and Planetary Sciences
Massachusetts Institute of Technology
Cambridge, MA 02139

Nancy J. House
EnCana Corporation
Denver, Colorado 80202

Abstract

Tight gas reservoirs are problematic to produce, often requiring multiple stages of hydraulic fracturing in order to create connected pathways through which hydrocarbons may flow. In this paper, we propose a new methodology to characterize the quality of hydraulic fractures. Using synthetic VSP and microseismic data, we test the concept that the rock volume containing open, gas filled fractures will scatter seismic energy more profusely than a volume containing closed, non-productive fractures. By measuring the amount of scattered energy in a time lapse 3D VSP study taken before and after the hydraulic fracturing episode, we hope to be able to compare the productive flow quality of different regions of the hydraulically fractured rock. The microseismic recordings allow us both to locate areas which have been hydraulically fractured and create imaging operators to extract the scattered signals from the time lapse VSP data.

1 Hydraulic Fracture Monitoring

In order to determine the extent of hydraulic fracturing away from the injection well, recordings of the micro-earthquakes made by the fracturing rocks are usually collected in a nearby observation well equipped with multiple levels of three component, clamped seismometers. The arrival times of these events are picked in near-real time and the location of the fracturing is determined using standard earthquake location technologies. To determine the exact location of each fracture requires a very accurate velocity model between the reservoir and the observation well. Because this is not generally known, events are located using a simplified velocity model giving at least relatively accurate positions. The hydraulic fracture program is then modified to make sure that the event locations are only occurring in the reservoir and not straying into the cap rock or the next well, for example. These events can then be co-rendered with a 3D seismic volume so that the lateral and vertical extent of fracturing can be visualized with interpretations of the reservoir unit. The effectiveness or quality of the fracturing is then measured by actual flow back tests into the well bore. While these tests can determine the overall success, it is currently not possible to isolate which specific portions of fractured rock volume are productive.

2 Seismic Scattering

Recent studies have shown that scattered energy from reservoirs with vertical fractures can be detected and characterized from surface seismic data (Willis et. al., 2006). This phenomenon is very different from subseismic cracks which cause velocity anisotropy and can be modelled by equivalent media theory. In contrast, scattering is caused by fractures which have dimensions about the same size as the seismic wavelength. These fracture systems scatter P and S wave energy which varies as a function of the illumination angle, specifically the difference in the acquisition and fracture

orientations. The amount of scattering is also affected by the tuning of the seismic wavelengths with respect to the fracture density and stiffness.

Hydraulically induced microseisms are frequently located in bands aligned with the maximum horizontal stress direction and reactivated pre-existing fractures. The purpose of our research is to investigate whether these induced fracture systems scatter seismic energy which could be observed in a 3D VSP survey. We present a model study which is motivated by a field data set from a tight gas field which was collected in the same manner as our model, i.e. a time lapse VSP and microseismic recordings of a hydraulic fracturing treatment.

3 Modelling of time-lapse VSP with a hydraulic fracture

To create synthetic VSP records, we used a 3-D elastic finite difference algorithm based on the rotated staggered grid method (Saenger and Bohlen, 2004; Zhang et al., 2006). The geometry of the model used is shown in Figure 1 and consists of five horizontal layers. All the layers are homogeneous and isotropic elastic media, with the third layer containing a hydraulic fracture with a single orientation. The fracture is represented by specific grid cells containing equivalent anisotropic medium parameters using the method of Coates and Schoenberg (1995). A single monitoring borehole containing 3-component receivers is shown in Figure 1 by the blue vertical line. The red stars show the surface seismic sources and the black square denotes the hydraulic fracture in layer 3. In concept this model is consistent with the actual field experiment that had one observation well and about 350 source points. In order to reduce the amount of computation time while simultaneously collecting a variety of source-receiver geometries, we recorded nine VSPs during each surface source simulation making a total of 91 VSPs created per model. The nine VSP observation wells were collocated under the surface shot positions.

For simplicity of presentation, we show only the results for the vertical velocity, Vz, component of the VSP well in the center of the model. Figure 2 shows the Vz component of energy for a) the case without any fracture, b) the case with a compliant, open fracture, and c) the case with a stiff, closed fracture. In each case, a 3x3 matrix is presented showing the traces from each of the 9 source locations, corresponding to the acquisition layout in Figure 1. From these figures the energy scattered off the facture can be seen most prominently for the compliant fracture case. This energy is also present in the stiff fracture case but is much lower in amplitude.

The time lapse, or difference plot, between the modelled VZ component of the VSP traces with and without a compliant fracture is shown in Figure 3a. The corresponding time lapse Vz component for the stiff fracture case is shown in Figure 3b. Since the only thing that has changed between the fractured and unfractured models is the small volume of the fracture itself, the energy in each time lapse VSP is simply the energy scattered from the compliant fracture. The volume of rock changed by the fracture should not be large enough to significantly modify the average velocities of the reservoir layer so the primary effect of the fracture will be to scatter the energy.

It is clear from these figures that there is a significant variation in the amount of scattered energy recorded in the observation well as a function of the direction of the illuminating source. The largest amount of scattered energy occurs when the source is normal to the fracture, as seen in the middle row of time lapse seismograms in Figures 3a and 3b. However, the non-normal illumination directions (rows one and two) still scatter significant amounts of energy. In every case, the scattered energy consists of both P waves, visible at the front end of the records, and S waves, which arrive later and have a slower move out across the traces. The proportion of S waves is much greater than that of the P waves, indicating that the fracture scatters energy most effectively as shear waves. Since the source used was an explosive, most of this energy must come from P to S conversions at the fracture itself.

The travel time from a surface shot location to the fracture is fixed based upon the velocity model. Figure 4 shows the idealized ray path, in red, from the shot (number 2) to the fracture. Shown in blue are the subsequent ray paths from the fracture to the observation well. Note that the path from the source to the fracture is the same for all receivers in the observation well, while the moveout seen across the receivers will be dictated by the travel paths from the facture itself. This fixed travel time from the source to the fracture will be different for each shot resulting in a static time shift between these time lapse VSP records. To this fixed travel time is added the time it takes to travel from the fracture back to each receiver in the observation well. Thus the moveout (i.e. the differences in arrival times) as a function of depth that we observe for each of these time lapse VSPs recorded at this observation well should be identical.

4 Using the microseismic events to extract scattered VSP energy

Figure 5 shows the idealized travel path, in blue, of microseismic energy from the hydraulic fracture to the observation well. Since the energy from the microseismic event travels only one way from the fracture to the observation well, its arrival time moveout will be identical to the time lapse VSP moveout, as shown in Figure 4, also in blue. Figure 6 shows a simulated microseismic event from the modelled fracture, using the same 3D elastic finite difference modelling algorithm we used to generate the VSP records. (Our goal is not so much to accurately model the microseismic trace, as to mimic the kinematics as it is recorded at the observation well. As such, Figure 6 uses an explosive source instead of a perhaps more appropriate double-couple source mechanism.) The first arrival on each trace is the P wave. The secondary arrival is the S wave. The observed microseismic moveouts of these P and S waves match the moveouts we see on the time lapse records (Figure 3). We can measure and record the arrivals of these events on the microseismic traces. So if we subtract the measured moveout of the microseismic event from the corresponding traces of the time lapse VSP, we will flatten the arrivals on the time lapse VSP traces. Note that the microseismic and VSP traces contain both P and S wave energy. This makes it possible to align both P and S wave scattered energy on the appropriate recorded components.

Figure 7 shows the time lapse VSP traces after removing the moveout of the microseismic P waves for a) the compliant fracture, and b) the stiff fracture. Figure 8 shows the time lapse VSP traces after removing the moveout of the microseismic S waves for a) the compliant fracture, and b) the stiff fracture. From these figures it is clear that the best discrimination between the P and S wave events is possible at the shallower depths. The arrival time moveout for receivers near the same depth level as the fracture is fairly flat giving little velocity discrimination between wave types. However, the arrival time of each wave type is clear. Simple ray tracing arguments show that when the fracture is located at different depths, there are still significant arrival time and moveout differences enabling the alignment and discrimination of the scattered energy. Additional separation techniques, like median, particle motion, and/or f-k filtering, can be applied to enhance the desired scattered energy.

In order to extract the energy scattered from the fracture on the aligned time lapse records we performed simple stacking of the traces. As mentioned above, since there is little velocity discrimination at the depth of the fracture, we stack only the shallow traces (<875m). This gives for each observation well, 9 stacked traces for each component of each surface shot. We perform the stacks separately for the P and S wave energy. On each stacked trace we compute the RMS energy of that wave type, based upon its arrival time. Since the P and S waves are present on all components (Vx, Vy and Vz) we combined the measured RMS energy for each wave type. So for each observation well we obtain 9 azimuthal measurements of scattered P wave energy and 9 corresponding measurements for S wave energy.

We perform this stacking operation for each of the nine observation wells for a total of 91 time lapse VSPs. We compute the RMS energy around the arrival time of the P and the S waves on each of the

stacked traces. So for each fracture type (i.e. compliant and stiff) we extract 182 measurements of scattered energy.

5 Scattered energy versus illumination direction.

Figure 9 shows the RMS value of the measured scattered energy as a function of the source illumination direction for 91 time lapse VSPs. We show for each azimuth the average of measurements for 9 VSPs. The energy extracted is in polar format displayed as a function of the difference in the source illumination angle and the fracture normal from a map view projection. (The actual angle of illumination is in three dimensions, but for simplicity we've chosen the two dimensional view from above.) Two different fracture models are displayed: one compliant and the other stiff. The compliant model represents the case of open, productive fractures. The stiff model represents closed, non-productive fractures. The top row shows the results for the scattered P waves and the bottom row shows the scattered S waves. The first column shows the average scattered energy for the compliant fractures. The second column shows the average scattered energy for the stiff fracture. The third column shows the ratio of the compliant to stiff scattered energy for the P waves (top) and S waves (bottom).

6 Will we really see the scattered energy?

The amount of scattered energy measured as a function of the illumination angle is related to the way the source energy interacts with the properties of the fracture. The first question is whether the scattered energy from the fracture is observable on the raw modelled VSPs and therefore likely to be extracted in the time lapse difference process. The scattered energy is greatest, and therefore most easily seen, on the records of the acquisition geometries where the sources and receivers are inline with the normal to the fracture surface. For the stiff fracture it is more difficult to see the scattered energy on the other, non-normal, raw VSP cases. For the compliant fracture case, the scattered energy is observable on nearly all the modelled raw VSP records. Depending on the actual fracture compliances in a reservoir, it is likely that we will be able to detect this energy. Of course, there is always the issue of how to optimally subtract the pre-fractured VSP data set from the post-fractured data to obtain the time lapse data volume. This is true for all time lapse studies and will need to be addressed in order to process the actual field data.

7 Can we use the microseismic data to extract the scattered energy?

The next question is whether our method of using the arrival times of the microseismic events to flatten and stack the time-lapse VSP data is effective for extracting the scattered energy. In our current implementation, the microseismic arrival times are hand picked. Additional automation can speed this up and make it practical to utilize the hundreds and perhaps thousands of microseismic events during a hydraulic fracturing treatment. On this model dataset, the use of the microseismic data to flatten the time-lapse VSP is effective for depths shallower than the fracture. Our simple implementation of a hand measured time shift does not take into consideration the potential phase or polarity mismatch between the microseismic and time-lapse VSP events. The phase term will need to be incorporated into the actual application of this method.

8 Can we discriminate between compliant and stiff fractures?

The last question is whether there are patterns in the scattered RMS energy analysis that will allow us to discriminate between the compliant and stiff fractures. The right column of Figure 9 shows that there is a difference of about a factor of five between the amount of scattered energy measured for the compliant and stiff fracture cases. This means that the economically important, open and compliant

fractures will scatter more energy than the less important, closed and stiff fractures. It is much more likely that the fractures contributing to permeability of the gas will be the ones which will scatter energy and be detectable by this method. On the other hand, the stiff, closed fractures are more likely to be invisible to our methodology. It may also be possible to discriminate between open and closed fractures by the azimuthal change in scattering as seen on the P and S wave RMS energy ratio plots. However, the measurement error on Figure 9 may seem to preclude the level of accuracy needed for this type of discrimination.

9 Conclusions.

We're proposing, in this model based study, a methodology to detect and characterize the quality of fractures which have been induced by hydraulic fracturing. We model the fractures as a thin band of anisotropic media which has properties related to the compliance of the fracture itself. The 3D time-lapse VSP data, taken before and after the hydraulic fracturing treatment, captures the scattered energy from the fractures. The recorded microseismic data allows us to create imaging operators to align and then extract the scattered energy. It also allows us to locate the fractured zone in the reservoir. While it is impossible to characterize the rock volume associated with each microseismic event, we expect that it will be fairly easy to compare the relative scattering for small rock volumes, perhaps as small as 50m on a side, across the reservoir. While the actual properties of the fractured zone itself may prove difficult to estimate, we should be able to map the areas with relatively higher fracture quality, i.e. open and compliant properties. We are currently extending this study to model multiple fracture systems and to include other filtering and stacking methods to more optimally extract the scattered energy from the time lapse data sets.

10 Acknowledgments

We would like to thank Rama Rao and Yang Zhang from MIT Earth Resources Lab as well as Julie Shemeta and Shawn Maxwell from Pinnacle Technologies Inc. for many helpful discussions about this topic. We thank Kent Willis from MIT for providing some of the software development support. We also thank the MIT ERL Founding Members and DOE grant DE-FC26-06NT42956 for funding this research.

11 References

Coates, R.T. and Schoenberg, M. [1995] Finite difference modeling of faults and fractures, Geophysics, 60, 1514-1526.

Saenger, E. H. and Bohlen, T. [2004] Finite-difference modeling of viscoelastic and anisotropic wave propagation using the rotated staggered grid, Geophysics, 68(2), 583-591.

Willis, M. E., Burns, D. R., Rao, R., Minsley, B., Toksöz, M. N. and Vetri, V. [2006] Spatial orientation and distribution of reservoir fractures from scattered seismic energy, Geophysics **71**, O43.

Zhang, Y., Campman, X., Grandi, S., Chi, S., Willis, M. E., Toksöz, M. N, Burns, D. R. [2006] F-K domain characteristics of the seismic response of a set of parallel discrete fractures, 76th SEG Annual Meeting Expanded Abstracts.

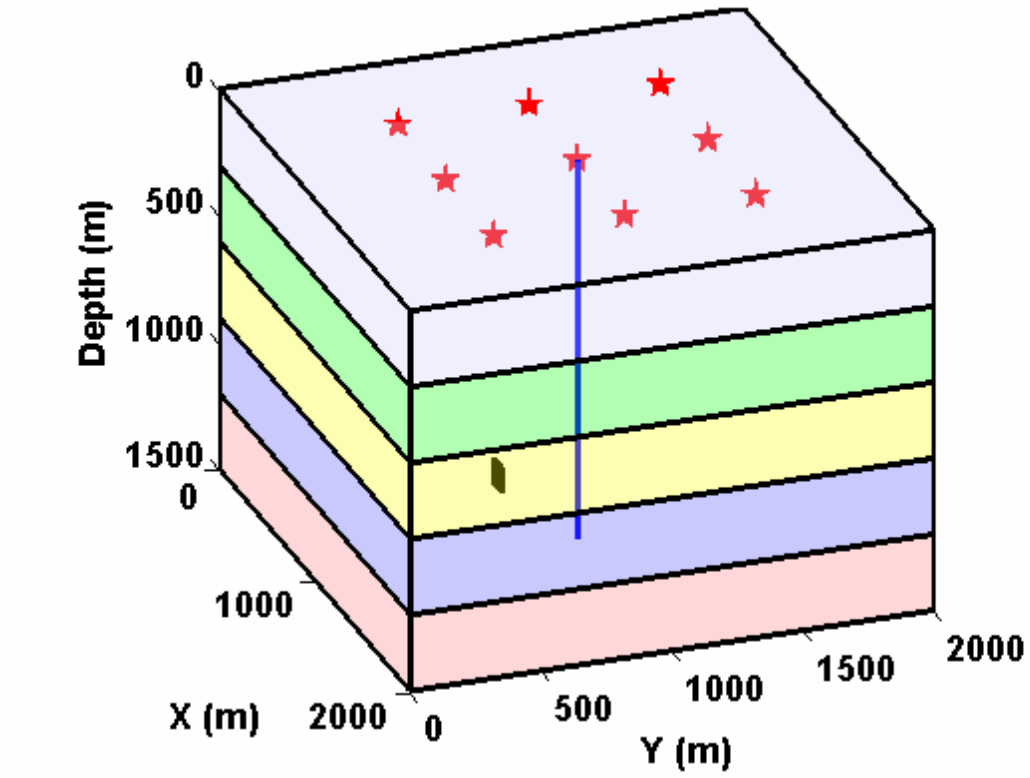

Figure 1a. Five layer model geometry showing one observation well (blue vertical bar), nine source locations (red stars), and fracture (black rectangle).

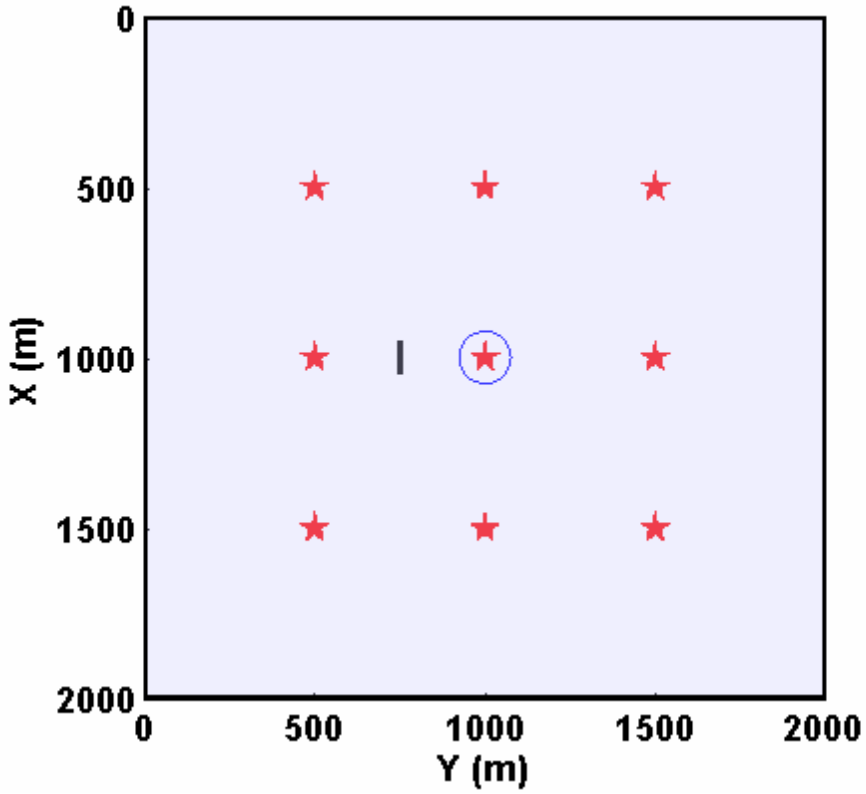

Figure 1b. Top view of model geometry showing observation well (blue circle), nine VSP shot locations (red stars) and fracture location (black line).

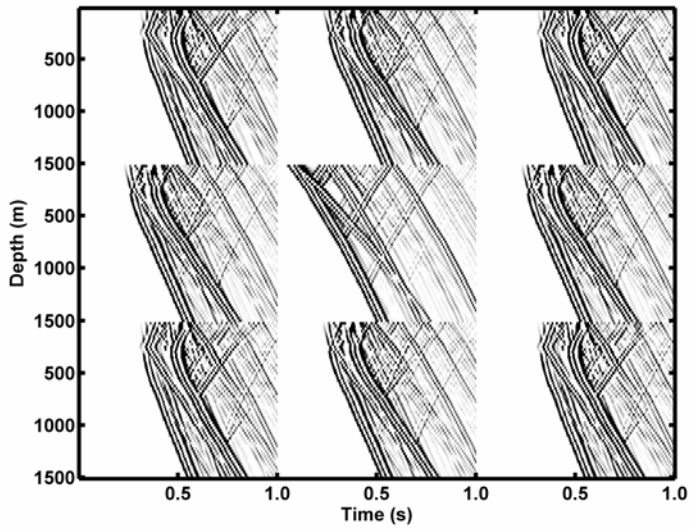

Figure 2a. Vz VSP traces recorded at the center observation well for each of the nine surface shots for a model which does not contain any fractures.

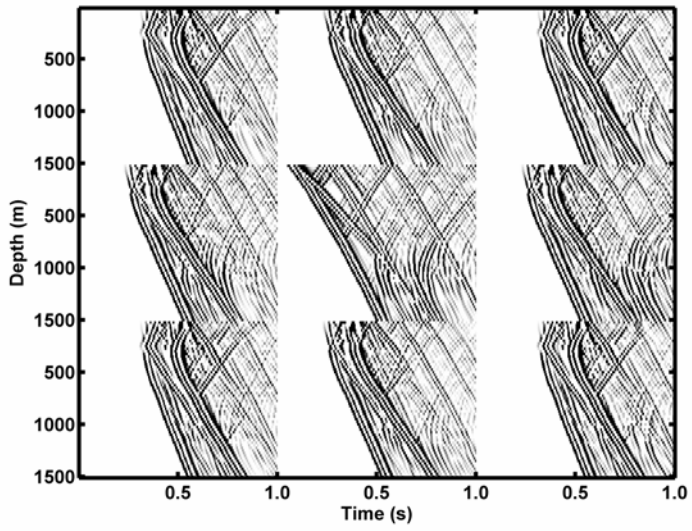

Figure 2b. Vz VSP traces recorded at the center observation well for each of the nine surface shots for a model which contains a compliant fracture.

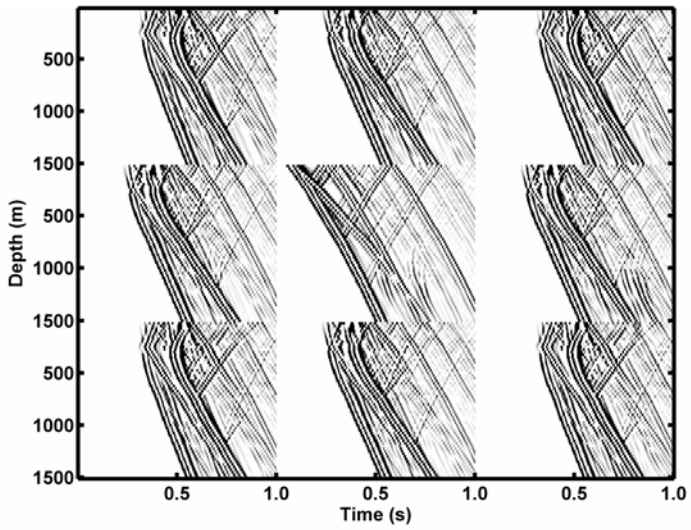

Figure 2c. Vz VSP traces recorded at the center observation well for each of the nine surface shots for a model which contains a stiff fracture.

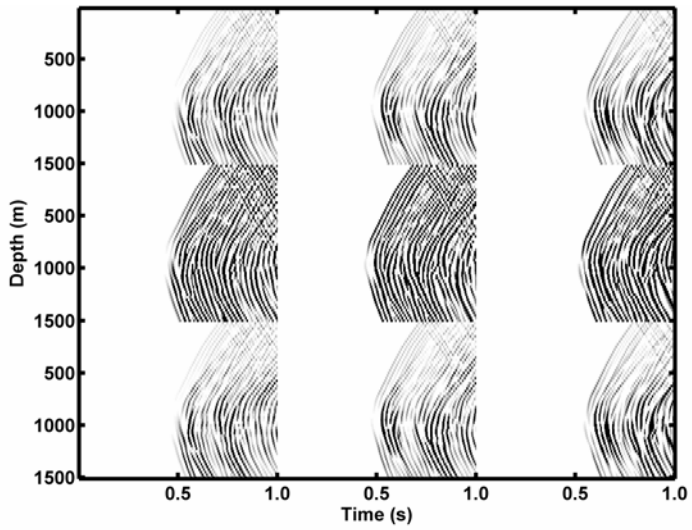

Figure 3a. Vz time lapse VSP traces recorded at the center observation well for each of the nine surface shots for a model which contains a compliant fracture.

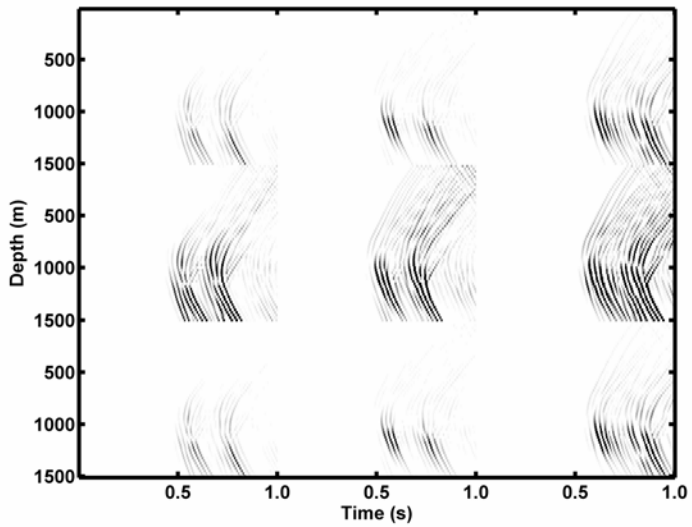

Figure 3b. Vz lapse VSP traces recorded at the center observation well for each of the nine surface shots for a model which contains a stiff fracture.

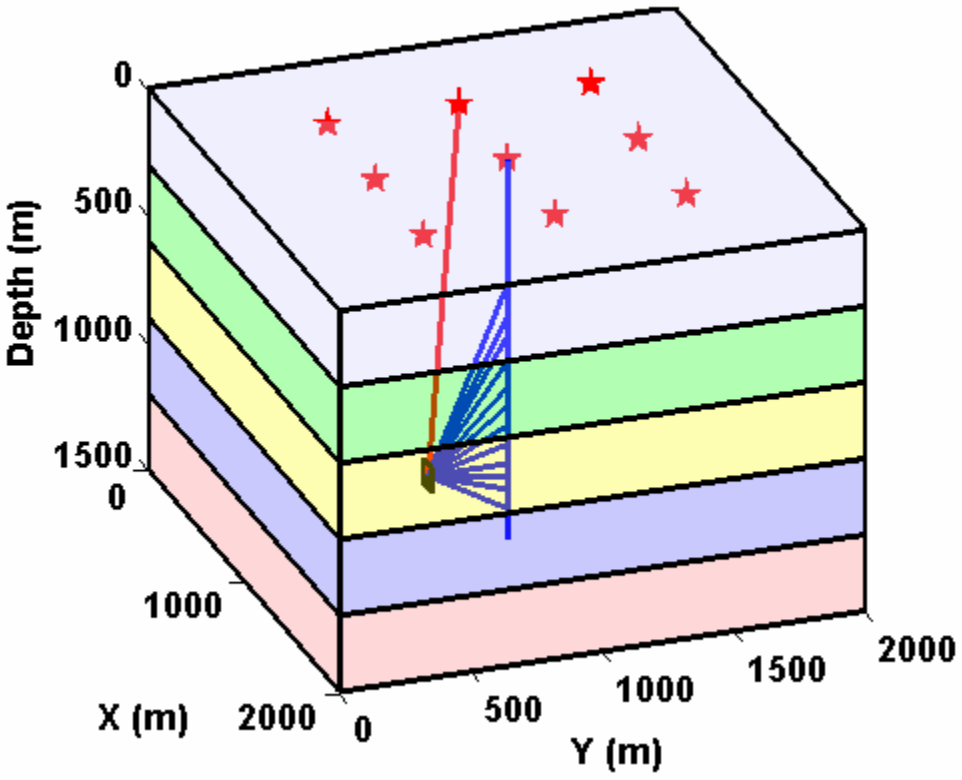

Figure 4. Left: five layer model geometry showing one observation well (blue vertical bar), nine source locations (red stars), and fracture (black rectangle). The red line shows the ray path from the source to the facture and the blue lines show the ray paths from the fracture back to the observation well.

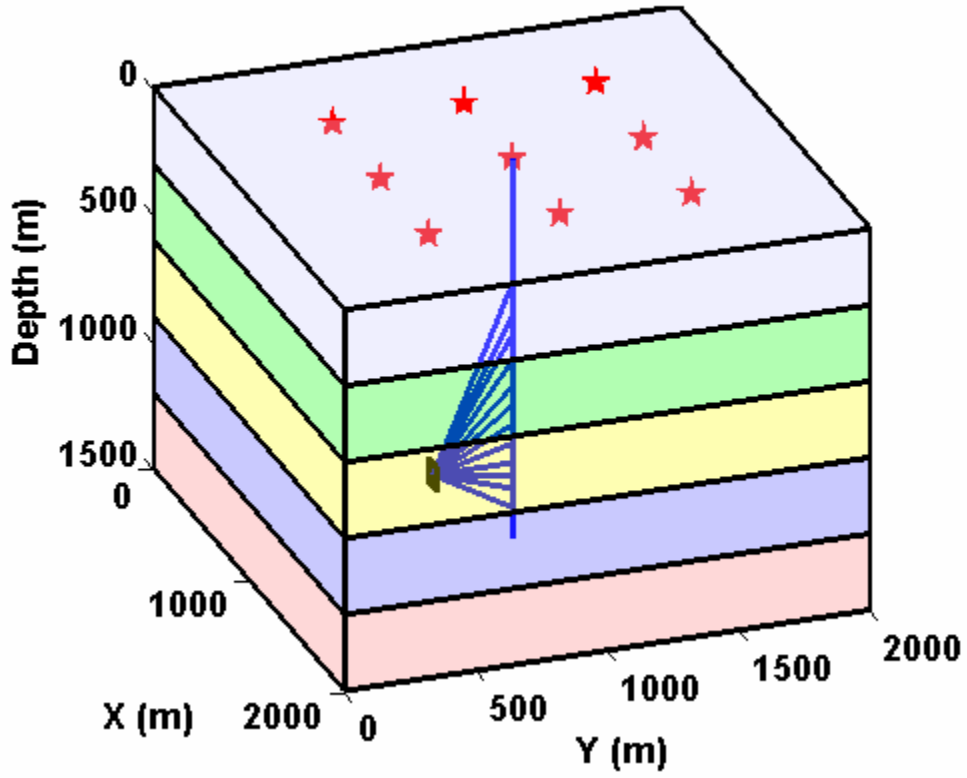

Figure 5. Five layer model geometry showing one observation well (blue vertical bar), nine source locations (red stars), and fracture (black rectangle). The blue lines show the ray paths from the fracture back to the observation well.

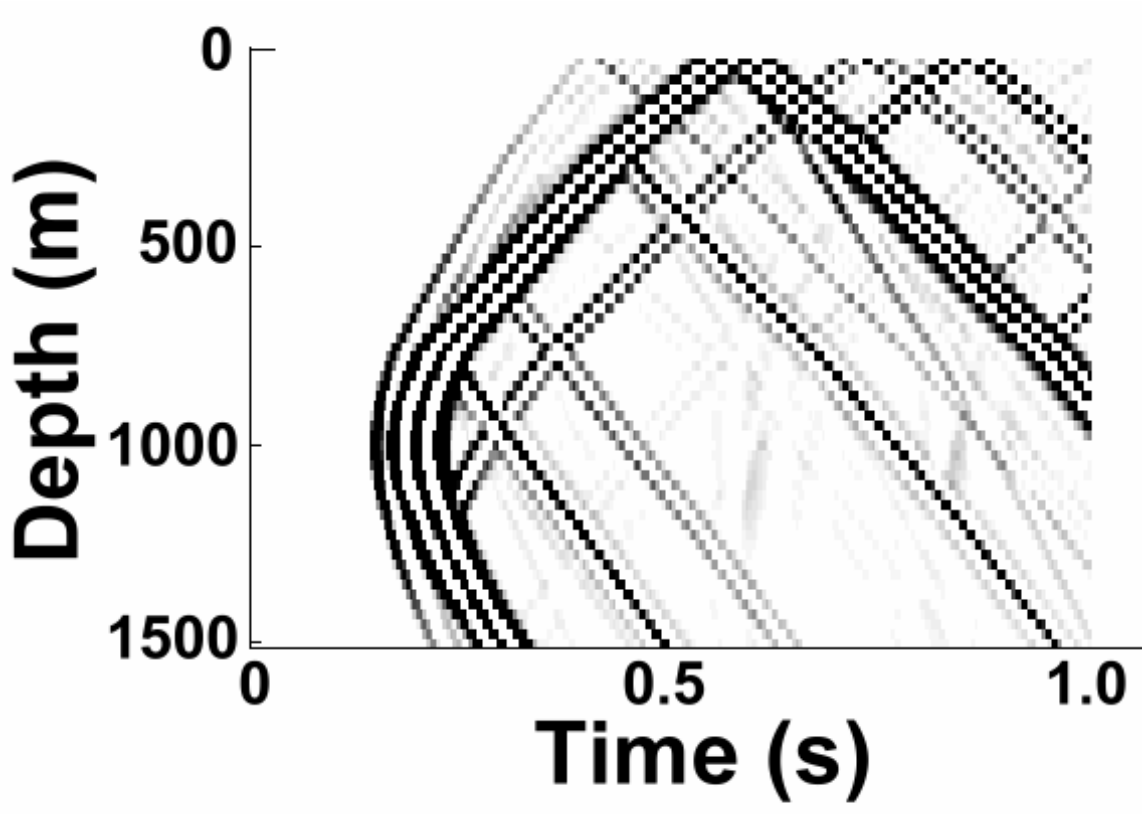

Figure 6. The simulated microseismic event recorded at the center observation well.

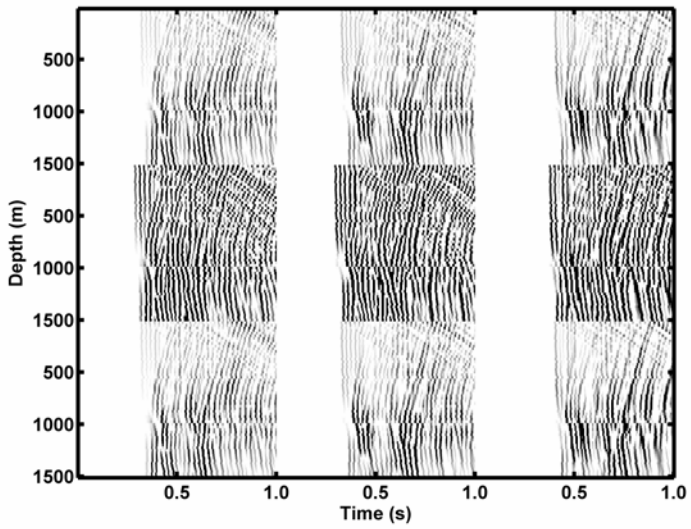

Figure 7a. Vz time lapse VSP traces, shifted with the microseismic P wave moveout, recorded at the center observation well for each of the nine surface shots for a model which contains a compliant fracture.

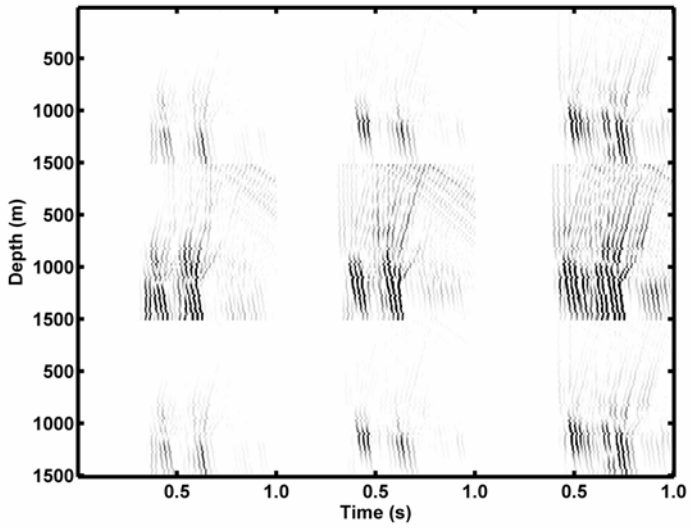

Figure 7b. Vz time lapse VSP traces, shifted with the microseismic P wave moveout, recorded at the center observation well for each of the nine surface shots for a model which contains a stiff fracture.

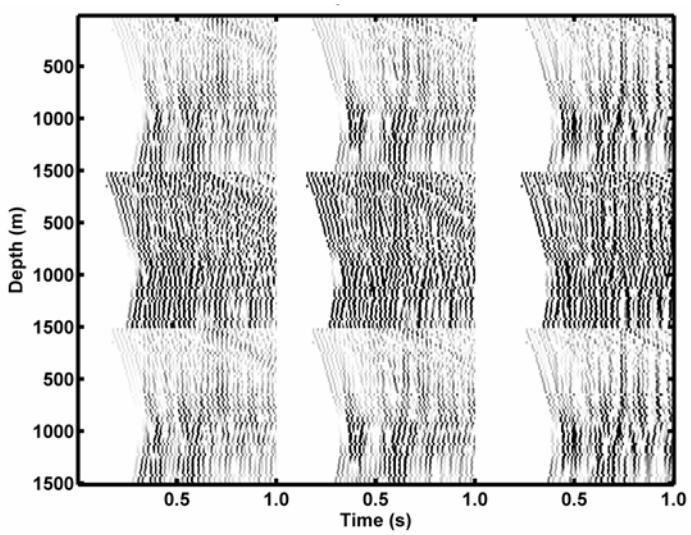

Figure 8a. Vz time lapse VSP traces, shifted with the microseismic S wave moveout, recorded at the center observation well for each of the nine surface shots for a model which contains a compliant fracture.

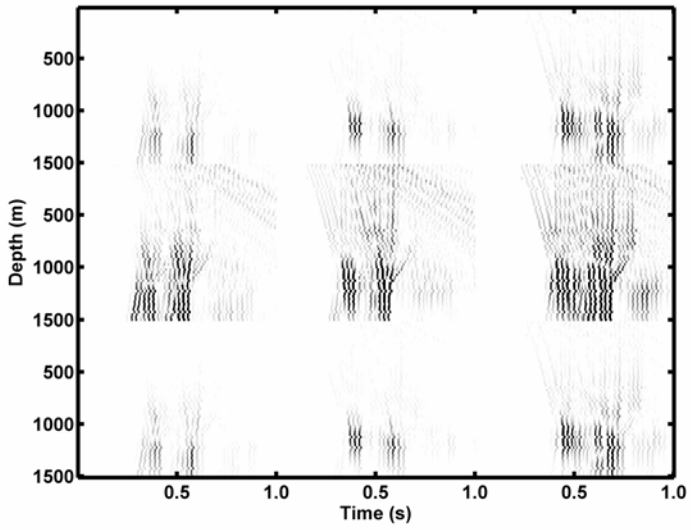

Figure 8b. Vz time lapse VSP traces, shifted with the microseismic S wave moveout, recorded at the center observation well for each of the nine surface shots for a model which contains a stiff fracture.

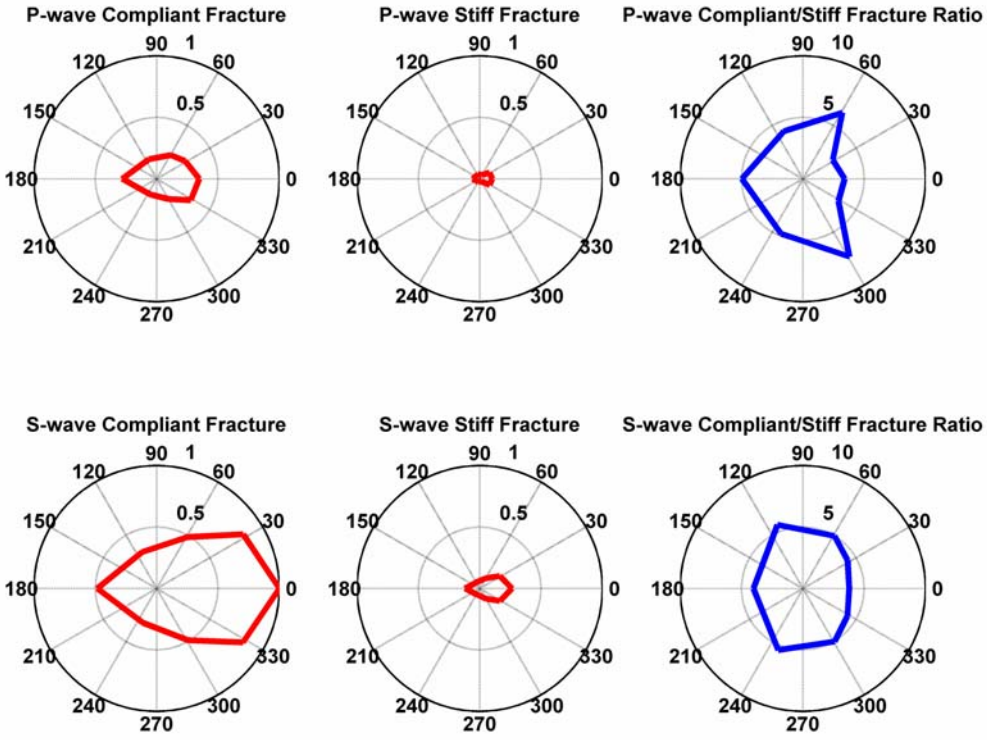

Figure 9. Polar plots of the average scattered P wave energy (top row) and S wave energy (bottom row) as a function of angle of incidence of seismic energy on the fracture. The compliant and stiff fractures results are shown in columns one and two, respectively. Column three shows the ratio of the Compliant to Stiff results. Note the 0 degrees azimuth denotes normal to the fracture strike.